Environmental Conditions Associated with Observed Snowband Structures within Northeast U.S. Winter Storms

Sara A. Ganetis and Brian A. Colle

School of Marine and Atmospheric Sciences, Stony Brook University, State University of New York, Stony Brook, New York

Sandra E. Yuter and Nicole P. Hoban

Department of Marine, Earth, and Atmospheric Sciences, North Carolina State University, Raleigh, North Carolina

ABSTRACT

Northeast U.S. winter storms commonly exhibit multiple meso-β-scale ($L < 200$ km) bands of enhanced radar reflectivity and precipitation. We use radar observations, upper-air soundings, and reanalyses from 108 cases of cool season (October–April) storms from 1996 to 2016 that occurred within the coastal corridor from Delaware to Maine to identify and assess various banding structures and environments. Banding can occur in several configurations among storms, and banding characteristics can differ at different times within the same storm. We classified 6-h storm periods as containing long (>200 km) single bands, single bands co-occurring with sets of mesoscale multibands, multibands only, and radar echoes without any bands using a combination of automated and manual methods. Use of radar reflectivity data at 0.5-dB precision and a variable rather than a fixed threshold showed that the occurrence of long single bands without any mesoscale multibands was rare, occurring in only 5 of 113 6-h periods. The most frequently occurring band configuration (55%) was concurrent single bands and multibands, which usually were present in the northwest quadrant of mature cyclones. Sets of multibands without a nearby single band usually occurred in the northeast quadrant of a cyclone poleward of weak midlevel forcing along a warm front. Overall, mesoscale single and multibands more commonly occurred after the cyclone occluded than in the developing stages. Multibands occurred in a wide range of frontogenesis and moist potential vorticity environments.

1. Introduction

Mesoscale banding within U.S. East Coast winter storms can lead to localized heavy snowfall rates and accumulations that can negatively impact lives and property within the heavily populated urban corridors of the mid-Atlantic and New England states. For example, the recent blizzard of 8–9 February 2013 exhibited an intense mesoscale snowband and resulted in power outages impacting 600 000 homes, over 6000 cancelled flights, and 18 fatalities (Krekeler 2013; Picca et al. 2014; Ganetis and Colle 2015). Winter storms exhibit bands with a variety of sizes, motions, and intensities, but most studies have investigated the primary band, or a single snowband with length $L > 200$ km (e.g., Novak et al. 2004; Kenyon 2013). In these previous studies, the use of radar data and mosaics based on level-III radar reflectivities with 5-dB steps made it difficult to discern the groups of

smaller, multiple bands with $L < 200$ km that also enhance snowfall accumulation. For example, the 26–27 December 2010 East Coast winter storm produced over 10 finescale (5–20 km wide and 10–100 km long) bands that led to over 6000 cancelled flights and disrupted regional train service (Soltow 2011; Kocin et al. 2011). A detailed analysis and comparison of the multiband environment with that of the single band within winter storms is needed to enhance understanding and prediction of these bands.

Mesoscale bands found within the comma head of developing and mature extratropical cyclones have been studied using conventional radar data for classification (e.g., Novak et al. 2004, 2010; Kenyon 2013). The primary band, hereafter referred to as a single snowband with $L > 200$ km, is typically found to the northwest of a surface low pressure center and coincides with the ascending branch of the ageostrophic frontogenetical circulation. This ascent and associated single band is narrowed and enhanced on the warm side of a midlevel frontal boundary in an environment

Corresponding author: Brian A. Colle, brian.colle@stonybrook.edu

with conditional symmetric instability (CSI) or weak moist symmetric stability (Emanuel 1985; Thorpe and Emanuel 1985; Xu 1989). Although single snowbands are the focus of many winter mesoscale precipitation studies (e.g., Sanders and Bosart 1985a,b; Wolfsberg et al. 1986; Novak et al. 2004, 2008, 2009, 2010; Novak and Colle 2012; Moore et al. 2005; Picca et al. 2014; Colle et al. 2014; Baxter and Schumacher 2017), smaller multibands, defined as ≥2 parallel bands with $L < 200$ km, are often found embedded within the comma head region of an extratropical cyclone and are less understood.

Although comparisons of case studies of banding within individual winter storms are prevalent in the literature (e.g., Nicosia and Grumm 1999; Jurewicz and Evans 2004), multiyear climatological studies consisting of >5 storms are less numerous. Novak et al. (2004) used mosaic radar reflectivity data to identify 88 cases from 1996 to 2001. Their study employed a subjective classification scheme of the reflectivity data that included single bands, narrow cold frontal rainbands, and multibands. They compared the environments between single bands and nonbanded cases and found that bands occurred to the northwest of a cyclone associated with a closed midlevel circulation with flow deformation and strong midlevel frontogenesis. The climatological study by Novak et al. (2010) aimed to isolate the role of moist processes in the evolution of the single-banded environment. Using the methodology from Novak et al. (2004), they identified 144 heavy precipitation cases from 2002 to 2008, and out of the 75 that exhibited a closed 700-hPa low, 30 single-banded cases were examined. Novak et al. (2010) utilized single, transitory, and null categories in the classification scheme with no separation of multibands. The main results of their study were that midlevel frontogenesis was stronger for banded events than null events, and conditional instability (CI) was more prevalent than CSI during single-band formation, which challenged previous studies.

Most band classification studies have relied on the human eye for band identification and classification (e.g., Novak et al. 2004, 2010; Kenyon 2013). The first automated continental United States (CONUS)-wide study of banded precipitation was created by Fairman et al. (2016). Using image processing methods on composite radar imagery, they found that for December–February from 2003 to 2014, the northeast United States experienced relative peaks in the banded precipitation in the Tug Hill Plateau of New York and lee of Lake Erie in western New York (likely associated with lake-effect precipitation bands) and within the Ohio Valley extending across the Appalachians to the coast of New Jersey (likely associated with banding within extratropical cyclones). This was a large-scale study focusing on banded features with a major

axis ≥100 km; therefore, smaller-scale bands, especially those embedded within the comma head of extratropical cyclones, were not addressed.

Climatological studies of bands have been conducted for storms impacting the Midwest and East Coast of the United States. A recent climatology of single-banded snowfall in central U.S. cyclones (between the Rocky and Appalachian Mountains) was conducted by Baxter and Schumacher (2017) using 1-km composite radar imagery for 66 cyclones exhibiting ≥4 in. (10.16 cm) of accumulated snowfall during five cool seasons from 2006 to 2011. Their study manually identified single bands that were ≥250 km long and defined events every 3 h within a storm. Out of the 66 cyclones, there were 98 banded events and 38 nonbanded events. The average snowband lasted 5.2 h and was 45 km wide and 428 km long. Out of the banded events, 54 occurred in the northeast (NE) quadrant relative to the cyclone center, 29 in the northwest (NW) quadrant, and 15 within both northern quadrants. Out of the 38 nonbanded events, the precipitation coverage occurred in both northern quadrants for 28 events. Their study differed from that of the East Coast winter storm analysis of Novak et al. (2004) in that this study found nearly twice as many nonbanded events, and more single bands formed in the NE rather than the NW quadrant.

One goal of this research is to create a multiyear dataset consisting of cool season (October–April) precipitation events that are identified and classified using predominately objective methods. This is the first time a formal study has applied an automated feature-based algorithm to determine snowband characteristics within a winter storm. This dataset can be compared with that of previous climatological studies that relied on manual classification methods. A potential caveat of using solely an automated method is that various fields, specifically radar reflectivity, can contain a wide range of values during one time in a single storm. Subjective methods were also employed in this work in order to achieve consistent classification among diverse storms.

Our paper aims to answer the following fundamental questions regarding single and multibands in the comma head region of extratropical cyclones in the northeast United States:

- What is the distribution of single bands, multibands, and nonbanded events identified using quasi-objective methods?
- How do vertical profiles of available moisture, instability, lift, and wind shear differ among multibands and single bands, as well as nonbanded precipitation areas in the comma head?

This paper is organized as follows. Section 2 describes the methods used to identify and classify precipitation

bands in northeast U.S. winter storms. Section 3 explores the cyclone relative band classification. Section 4 discusses the thermodynamic environment of the various classifications of precipitation bands with a focus on contrasting known banding environmental ingredients (i.e., moisture, instability, lift). Finally, section 5 summarizes the main results of this banding study.

2. Data and methods

a. Case identification

Cases were identified as cool season (October–April) low pressure systems that tracked through the northeastern United States (NEUS) between 1996/97 and 2015/16 with ≥1.00 in. (2.54 cm) of liquid equivalent snowfall measured at ≥2 of 7 Automated Surface Observing System (ASOS) stations across the NEUS (Fig. 1), which consisted of Portland, Maine; Islip, New York; Boston, Massachusetts; Philadelphia, Pennsylvania; Bridgeport, Connecticut; Providence, Rhode Island; and Newark, New Jersey (Hoban 2016). Over 150 cases were initially identified using this metric over 20 cool seasons, but 108 were ultimately used based on radar data availability from six coastal radars (Fig. 1). Each case could span multiple days, depending on the speed and extent of the affecting cyclone, but such days were consolidated into a single case within the database.

b. Cyclone tracking

The band location relative to the surface cyclone center [i.e., nearest sea level pressure (SLP) minimum] is used in this study to provide a storm relative framework and to compare with recent studies that highlight single bands that form in the northwest quadrant for NEUS storms (Novak et al. 2004) or the northeast quadrant for CONUS storms (Baxter and Schumacher 2017). The sea level pressure data for the cyclone tracks were obtained from the 6-hourly 0.5° NCEP Climate Forecast System Reanalysis (CFSR; Saha et al. 2010) for years they were available (1996–2010) and then from the 6-hourly 0.5° NCEP Climate Forecast System version 2 (CFSv2; Saha et al. 2014) analyses (2011–16). Other reanalysis data were considered, including the North American Regional Reanalysis (NARR). Charles and Colle (2009) showed that the NARR had a weak sea level pressure bias for cyclones along the U.S. East Coast that was not shown with the CFSR (Colle et al. 2013). Thus, the CFSR was used in favor of the NARR.

To track the extratropical cyclones on a common grid, the Hodges (1995) cyclone tracking scheme was
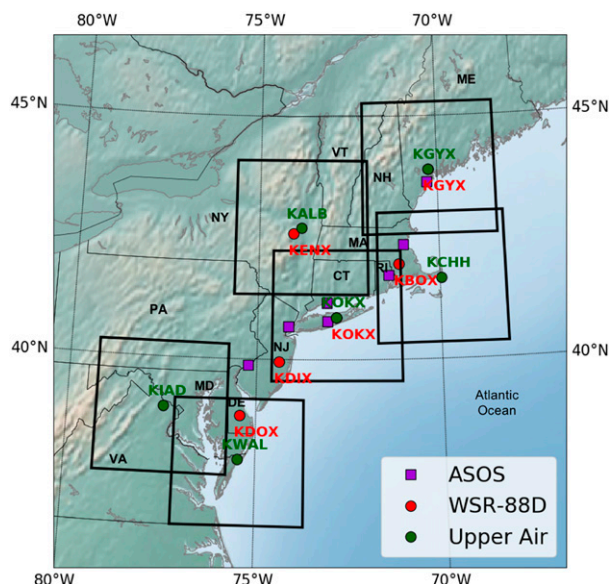

FIG. 1. Map showing locations of six upper-air sites (green circles) used for vertical profiles through regional classification given by each box bounding ~150 km around the upper-air site. Locations of regional NWS WSR-88D radar (red circles) and ASOS sites (purple squares) are shown.

implemented according to the methodology provided by Colle et al. (2013). Storms must track at least 1000 km and have a lifetime of ≥24 h. The distance and lifetime criteria are employed to remove features that are too short-lived or remain too stationary. If there were multiple cyclones in the NEUS domain for a particular case, the cyclone subjectively determined to be more associated with the observed precipitation, as shown by the radar reflectivity regional composite discussed in section 2c, was manually selected. If a cyclone track did not appear for a particular case because the cyclone was too weak to be identified, then the NOAA Weather Prediction Center (WPC) surface analyses for that date and time were used to subjectively track the manually identified low pressure center every 6 h. This supplemental method was used for two storms. The cyclone tracks for each case used in this study are shown in Fig. 2.

c. Regional composite radar dataset

The radar data processing methods are described in detail by Hoban (2016) and Corbin (2016) and are summarized in this section. Level-II data from each of the six radars (KGYX, KENX, KBOX, KOKX, KDIX, and KDOX in Fig. 1) were downloaded from the National Centers for Environmental Information (NCEI) radar archive and quality controlled to remove nonmeteorological echoes within individual elevation
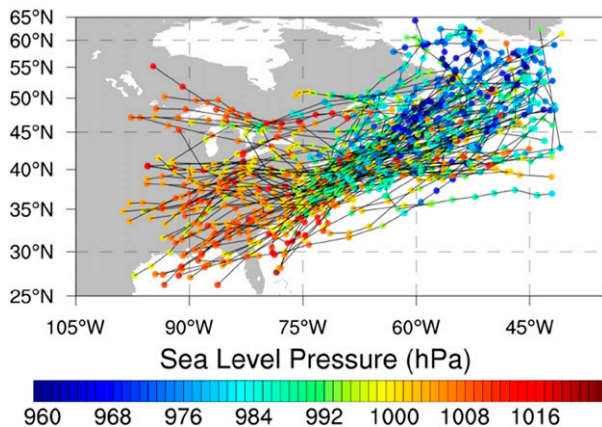
FIG. 2. SLP along each of the 108 cyclone tracks in the study with points along the track colored by SLP, with warmer colors indicating weaker cyclones and cooler colors indicating stronger cyclones.

angles in polar coordinates. Analysis of overlapping echo regions at equal distances between adjacent radars was used to apply a relative radar reflectivity calibration with respect to KOKX observed values. KOKX was used because it is close to the center of the study domain. The polar coordinate data were then interpolated to a 2 km × 2 km Cartesian grid at a constant elevation of 2 km AGL, extending to a 200-km radius from each site for every 6–10 min during each storm. For the duration of each storm, regional maps of radar reflectivity were constructed by regridding each volume scan to a common 801 km × 801 km grid with 2-km horizontal grid spacing. Since the timing of volume scans among radars was not synchronized, KOKX was used as the central reference radar, and data from the other five radars were used as long as their volume start time was within 8 min of the volume start time at KOKX. There are sometimes gaps in the regional maps when data from an individual radar were not available in the NCEI archive. This analysis uses 5-min level-II radar reflectivity data (0.5-dB precision) for every volume scan ±1 h from a 6-hourly analysis time during the storm. An important distinction between this study and previous studies such as Novak et al. (2004) and Kenyon (2013) is that they used level-III radar reflectivity data (5-dB precision).

d. Objective identification of bands

Precipitation bands are classified from automatically detected objects from the gridded reflectivity data. The Method for Object-Based Diagnostic Evaluation (MODE) tool within the Model Evaluation Tools (MET) version 5.1, developed at the Developmental Testbed Center (DTC) at the Research Applications Laboratory

(RAL) at the National Center for Atmospheric Research (NCAR), was used to objectively identify precipitation structures in the stitched regional composite radar data (Developmental Testbed Center 2015; Davis 2006a,b; Brown et al. 2007; Bullock et al. 2016).

Masking using an adaptive threshold was used to identify candidate objects with locally enhanced radar reflectivity, which were then filtered based on geometric attributes to classify large bands, midsized bands, and undefined enhanced reflectivity regions. Masking was used to create a binary field that equals 1 above the threshold and 0 elsewhere. The adaptive threshold value for the reflectivity field varies during each case. Lawson and Gallus (2016) found that objective identification and verification of reflectivity data exhibited substantial sensitivity to the reflectivity threshold chosen for summertime convection. They found that using too low of a reflectivity value (5 dBZ) yielded a sample size of objects that was too small, but using too high of a value (40 dBZ) lost other features (i.e., stratiform precipitation). They concluded that the threshold chosen should be done so to focus on the feature of interest. In a study of banding throughout all four seasons, Fairman et al. (2016) chose a static threshold value of 20 dBZ.

In this study, the adaptive threshold for each case resulted from a series of tests on 10 example cases. Bulk statistics were computed from the regional composite reflectivity data for both the entire storm duration and for individual 5-min times during the storm. The following quantities were calculated: minimum, lower decile, lower octile, lower quartile, median, mean, upper quartile, upper octile, upper decile, and maximum. Data were used throughout the entire regional radar composite domain and also tested on a subregion centered over Long Island, New York.

The adaptive threshold that was found to work best for the 10 cases was the upper sextile of the reflectivity throughout the NEUS domain at *each* time within a storm. That meant that 17% of the reflectivity data are at or above this value, therefore highlighting the enhancements of snowbands within the weaker, smaller reflectivity values. The upper quartile was found to be too low and failed to separate individual bands of higher reflectivity embedded within widespread precipitation. The upper octile was found to be too high of a threshold that trimmed bands down, therefore underestimating their spatial characteristics. The upper-sextile threshold calculated at each time step performed best at separating out individual multibands from nonbanded precipitation and any nearby large bands and was used to create the masked field.

Once the masked field is computed, objects are identified with the MODE tool as regions that are continuous in space. If there is even one grid point separating the objects, they are identified as separate objects. Attributes are computed for each object and include the object area, which is the number of grid squares an object occupies, and the centroid, or geometric center, of an object. The length, width, aspect ratio, and axis angle are computed by fitting a rectangle around each object. The aspect ratio is the ratio of the short axis to the long axis. The axis angle is the angle of the long axis of the rectangle relative to 90° (east).

There is a large variation of storm (and reflectivity) intensity among all 108 storms that ultimately motivated the time-varying adaptive threshold. However, this time-varying threshold was not without its limitations. There were times when a weaker band existed during a stronger storm with too high a reflectivity threshold that resulted in a failure of the method. The threshold was skewed higher by offshore rain in several storms when a portion of the storm was over warm Gulf Stream waters. Ultimately, the objective method did not work well for eight out of 108 storms, during which manual methods had to be employed to subjectively identify (i.e., use the human eye on the raw observed reflectivity field) instead of rely on the objective methods for five cases of both a single band with multibands and three cases of multibands only.

e. Classification of bands

Classification was first completed by postprocessing the data output from MODE. Objects were determined to be snowbands if their aspect ratios (length of minor axis divided by the length of major axis) were ≤0.5. The bands were additionally classified into large bands, midsized bands, or undefined, according to the length and width criteria provided in Table 1.

Next, both the classified field and the raw reflectivity field were analyzed to subjectively classify dominant banding types at each 6-hourly analysis time during a case (i.e., 0000, 0600, 1200, and 1800 UTC). The classifications were one of four different categories based on the types of objects that were identified ±1 h of the analysis time within one boxed sounding domain extending 150 km from each of the six sounding locations in Fig. 1 (i.e., KGYX, KALB, KCHH, KOKX, KIAD, and KWAL) every 6 h during a case. An event was classified if the radar echo was found in ≥50% of the sounding domain box for ≥2 h. The use of 6-hourly events is consistent with what had been done in previous studies (e.g., Novak et al. 2004; Baxter and Schumacher 2017). The four storm-band categories (Table 2) were adapted from Novak et al. (2004, their

TABLE 1. Criteria used to objectively classify objects output from the MET MODE tool applied to stitched regional composite reflectivity data.

	Length L	Width W	Aspect ratio (W/L)
Large band	$\geq 200\,\text{km}$	$20 \leq W \leq 100\,\text{km}$	≤ 0.5
Midsized band	$< 200\,\text{km}$	$10 \leq W \leq 50\,\text{km}$	≤ 0.5
Undefined/cell	$10 \leq L \leq 100\,\text{km}$	$10 \leq W \leq 100\,\text{km}$	> 0.5

Table 1). The first category is for a storm that exhibits a large band ($L \geq 200\,\text{km}$) and no other identified structures in the sounding domain and is termed the "single band" category (SINGLE; sample size = 5). The second category is for a storm that exhibits ≥2 midsized bands that are parallel to each other and move similarly in the sounding domain and is termed the "multiband" category (MULTI; sample size = 35). The third category is for a storm that exhibits a large band accompanied by midsized bands and is termed the "both single band and multiband" category (BOTH; sample size = 107). In the analysis below, we examine separately the environment of the large band (BOTH–Large bands) and concurrent multibands (BOTH–Midsized bands). The fourth and final category is for storms that exhibit none of the previous linear precipitation structure classification criteria and is termed the "nonbanded" category (NONE; sample size = 46). Figure 3 shows examples of cases in each of the four categories.

f. Subjective classification of banding events for cyclone stage and movement

Storms were additionally subclassified based on both cyclone stage and band motion. Cyclone maturity has been used in refining climatological studies, such as by Novak et al. (2010), who used the presence of a closed 700-hPa circulation to differentiate comma head cases (i.e., stronger cyclones that would likely have precipitation wrapping around the center to form a comma head) from non-comma-head cases within their 6-yr study. Kenyon (2013) looked into band motion with a special focus on both laterally translating and radially pivoting single bands.

Cyclone maturity during each 6-h time was classified as either developing or mature, determined manually using the WPC surface analyses following the Norwegian and Shapiro and Keyser cyclone models (Bjerknes and Solberg 1922; Shapiro and Keyser 1990; Colle et al. 2014). Specifically, developing storms were defined as having an open wave frontal structure while mature cyclones were at the start of the occluded

TABLE 2. Case classification by band type, cyclone stage, and band motion for 6-hourly events during banded cases.

Classification	Cyclone stage	No. of events with band movement perpendicular (parallel) to the long axis of the band
Single band only	Developing	0 (0)
	Mature	3 (2)
Multibands only	Developing	6 (12)
	Mature	14 (3)
Both single and multibands	Developing	15 (28)
	Mature	58 (6)
Nonbanded	Developing	29
	Mature	17

stage, defined as when circulations around a cyclone create an occluded front that separates the cold air behind the cold front from the warm air ahead of the cold front (Schultz and Vaughan 2011). The location of the precipitation band relative to the cyclone center can depend on cyclone maturity, such as forming north of a warm front in a developing cyclone versus northwest along the occluded front in a mature cyclone (Schultz and Vaughan 2011). The four storm-band categories were further classified into developing and mature cyclones, resulting in eight categories.

The 5-min interval animations of reflectivity and classified bands were used to classify geographic-centric band motion by animating ±1 h on either side of the 6-hourly analysis time. Band motion with respect to the long axis of the band was assessed. One or more bands were classified as moving perpendicular or parallel to their long axis or axes. The perpendicular classification is comparable to the laterally translating and pivoting classifications used by Kenyon (2013). The parallel classification is comparable to the laterally quasi-stationary classification used by Kenyon (2013). The results from their study showed that various band motions resulted from different synoptic and mesoscale environments; therefore, they were taken into account within this study for comparison. The eight classifications of band type and cyclone strength were further subclassified into perpendicular- and parallel-moving bands, resulting in
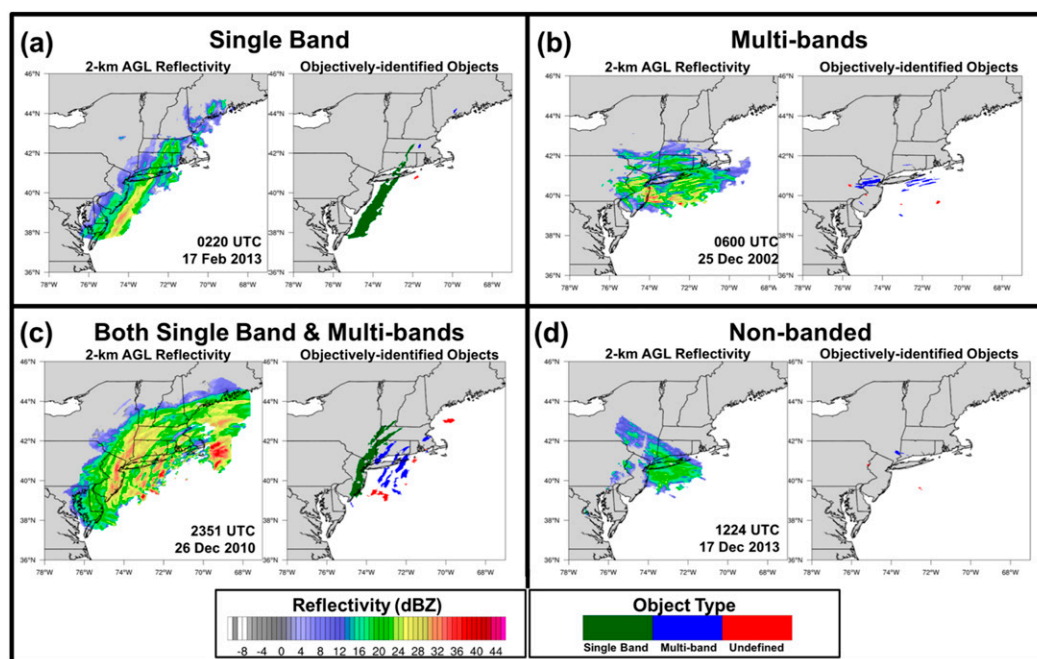

FIG. 3. Examples of 2-km AGL stitched regional composite reflectivity and the resulting classified objects from the MET MODE tool output for the four banding classifications exhibited in NEUS winter storms: (a) a large, single band, (b) multibands, (c) both single and multibands, and (d) nonbanded.
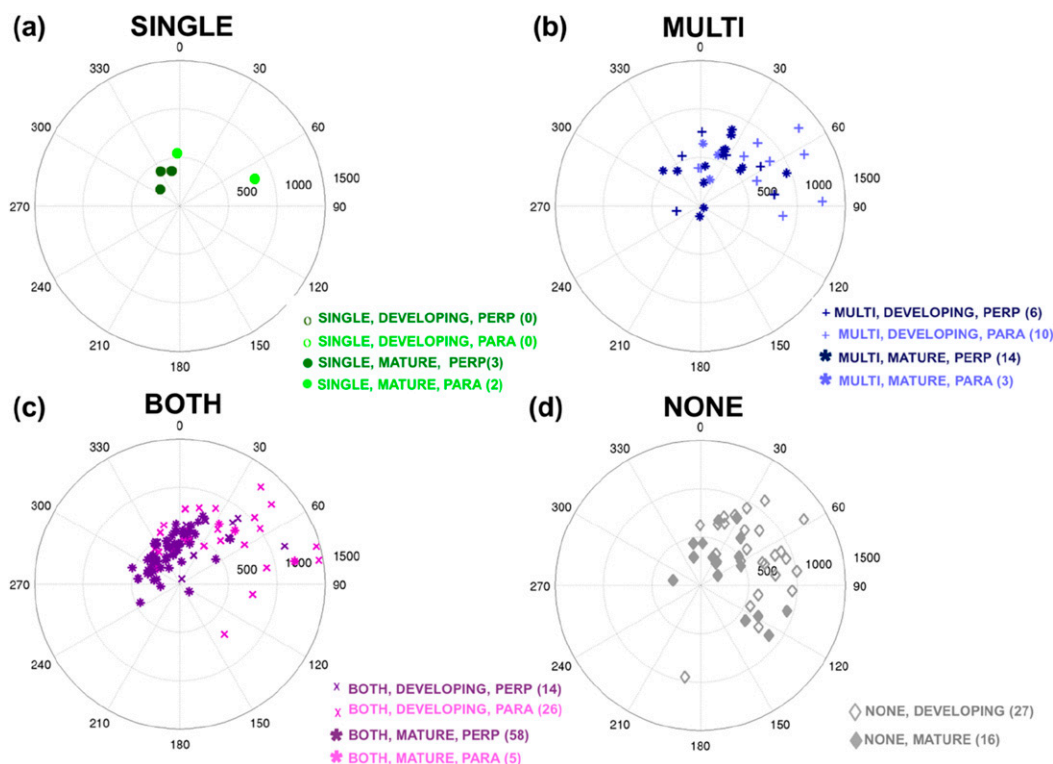
FIG. 4. Distance and angle from cyclone low pressure center for 193 events for (a) SINGLE events for mature (filled circle) and developing (open circle) cyclones for parallel-moving bands (light green) and perpendicular-moving bands (dark green); (b) MULTI events for mature (asterisk) and developing (plus sign) cyclones for parallel-moving bands (light blue) and perpendicular-moving bands (dark blue); (c) BOTH events for mature (asterisk) and developing (cross) cyclones for parallel-moving bands (light purple) and perpendicular-moving bands (dark purple); and(d) NONE events for mature (filled diamond) and developing (open diamond) cyclones. The radial distance is in km, and the angle from the cyclone to the sounding location at the center of the domain of the classified event is in degrees.

12 different classification categories. The nonbanded (NONE) classification was classified into developing or mature cyclones, but no motion criteria were applied because there were no defined bands to base the classification on.

g. Analysis of band environment

Observed soundings from the six upper-air locations over the northeast United States are available approximately every 12 h (Fig. 1). To increase the temporal frequency of available vertical profiles to every 6 h, vertical profiles were also derived from the 0.5°-resolution CFSR. These are the same analysis data used by Kenyon (2013) for their environmental band analysis. The CFSv2, which was used for dates later than 2010, has data approximately every 38 km horizontally with 64 vertical pressure levels (Saha et al. 2014). Our analysis focus is above the boundary layer, thus minimizing the effect of terrain or surface type differences.

The accuracy of these CFSR gridpoint profiles was determined by comparing 1292 available soundings every 6 h during each of the 108 events from the six coastal sites (Fig. 1). Above the boundary layer (>2 km AGL), the mean error of temperature was typically ±2°C and relative humidity ±15%. The mean errors for mixing ratio above the boundary layer are typically within $\pm 1\,\mathrm{g\,kg^{-1}}$ and are within ±2 K for potential temperature. Based on this evaluation, the CFSR-derived soundings were considered a reasonable estimate to the observed atmosphere for the purposes of our analysis.

Each 6-h event corresponds to bands (or lack thereof) within one specific domain that is centered on and extends ~150 km from a sounding site (Fig. 1). Vertical profiles based on 6-h CSFR reanalysis were taken at the nearest grid point to MODE-identified band centroid (see sections 1d and 1e) within a sounding domain. For times during which multibands were identified, profiles were taken from each

individual midsized band. For times during which both large bands and midsized bands were observed, profiles were taken from the large band (BOTH–Large bands) and any available midsized band (BOTH–Midsized bands) separately. For nonbanded events, the center of the sounding domain was used for the profile extraction.

3. Cyclone-relative band classification

Distribution by event

The results of the approximately 6-hourly event classifications produced a total of 193 events from the 108 cases. The distribution of the sounding domain of each classification relative to the cyclone center is provided in Fig. 4. The initial classification into the four standard categories is as follows: five SINGLE, 35 MULTI, 107 BOTH, and 46 NONE. All five SINGLE events were associated with a mature cyclone, and most occurred in the northwest quadrant of a cyclone (Fig. 4a). MULTI events were approximately equitably distributed between developing (18) and mature (17) cyclones. BOTH events were less often observed with developing (43) than mature cyclones (64). NONE events were more often associated with developing (29) than mature cyclones (17). The results of the final application of the geographic-centric band movement classification are provided in Table 2. While the distribution of counts of MULTI events was similar for both developing and mature cyclones, the bands favored parallel movement when associated with developing cyclones versus a perpendicular movement when associated with mature cyclones. For both mature and developing cyclones, more multibands occurred in the northeast quadrant than the northwest quadrant (Fig. 4b). A similar relationship for band motion is evident when comparing the motion associated with BOTH events. Parallel band motion is predominant during developing cyclones versus perpendicular motion during mature cyclones. Perpendicular-band-motion-classified events typically occurred in the northwest quadrant of a mature cyclone, while parallel-band-motion-classified events typically occurred in the northeast quadrant of a developing cyclone (Fig. 4c). Nonbanded events were predominantly in the eastern quadrants, favoring the northeast quadrant (Fig. 4d).

Figure 5 shows the band orientation in addition to the location relative to the cyclone center for large bands from SINGLE and BOTH events for developing and mature cyclones. There is a cluster in the northwest quadrant of bands oriented southwest–northeast,
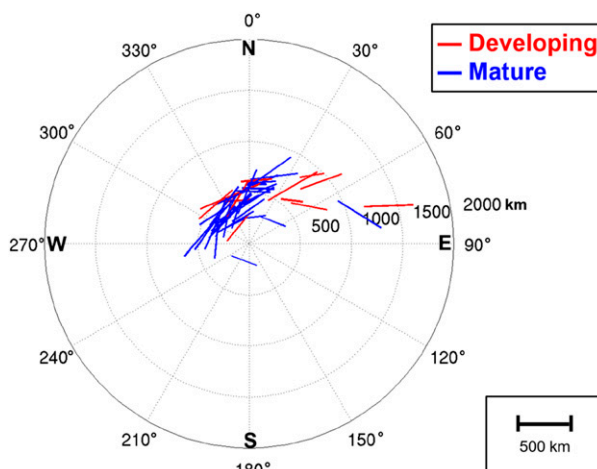

FIG. 5. Large-band locations and orientations relative to the cyclone center (origin of plot), with the radius in km and angle in degrees. Bands associated with mature cyclones are in blue, and developing cyclones are in red.

which is observed to match the orientation of enhanced baroclinic zones that will be analyzed in section 4. More large bands ≥500 km from the cyclone center in the northeast quadrant are associated with developing cyclones (7) rather than mature cyclones (2). The more west–east orientation of these large bands is thought to be due to their collocation with the warm front. The band orientations and clustering in the northern quadrants is consistent with similar analysis conducted by Novak et al. (2004) and Baxter and Schumacher (2017).

4. Vertical profile analysis

Comparisons of the thermal, moisture, and kinematic variables from a representative profile from 1000 to 300 hPa from each event were examined. Significance is assessed via bootstrapping (Wilks 2011); each classification dataset is resampled by replacing randomly 1000 times. For all four datasets, the size for each resample is equivalent to the total number of events in the original dataset (5 SINGLE, 35 MULTI, 107 BOTH–Large bands subset, 107 BOTH–Midsized bands subset, and 46 NONE).

Given the common location within the comma head of a cyclone, there is little variation in temperature profiles among the four classifications (Figs. 6a–f). There was some variability in the presence of an unsaturated layer, which is the most pronounced in the SINGLE classification (Figs. 6f–j). Individual profiles of saturation equivalent potential temperature (θ_e^*) show the presence of weak conditional stability indicated by a small increase in θ_e^* with
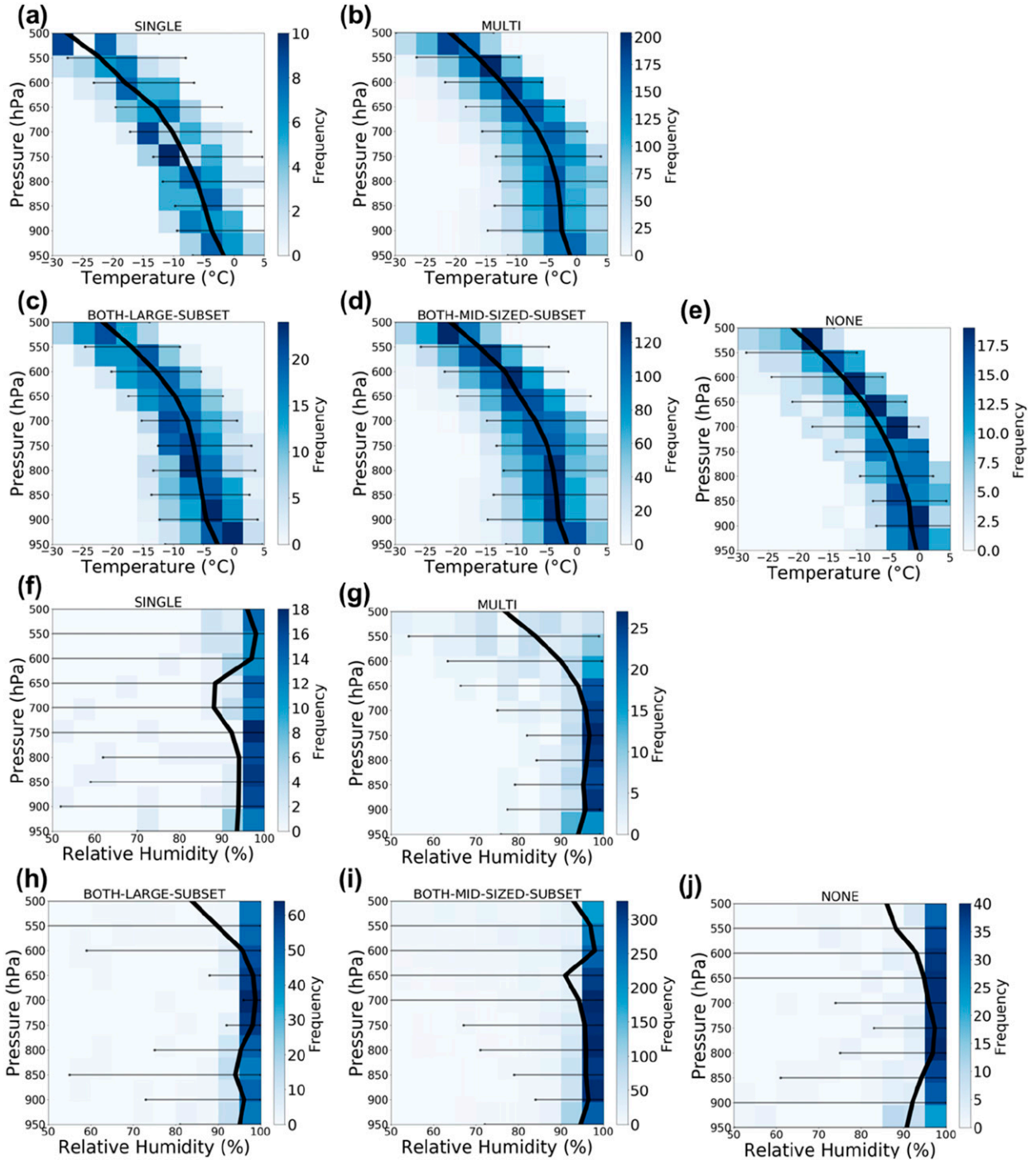
FIG. 6. Vertical profiles of (a)–(e) temperature (°C) and (f)–(j) relative humidity (%) for events classified as (a),(f) SINGLE; (b), (g) MULTI; (c),(h) BOTH–Large bands subset; (d),(i) BOTH–Midsized bands subset; and (e),(j) NONE events. Bold lines denote the mean profile for each classification, with markers indicating 2.5nd and 97.5th percentiles of the mean with 95% confidence.

height for all classifications (Figs. 7a–e). Over 20% of SINGLE and BOTH–Large bands profiles exhibited a 50-hPa-deep conditionally unstable layer (≤ -0.02 K hPa^{-1}) compared to <5% of MULTI and

BOTH–Midsized bands (not shown). The MULTI and BOTH–Midsized bands events have larger average wind shear (950–750 hPa) values, ~5.8 and 5.67 m s^{-1}, respectively, compared to the ~3.7 and ~3.0 m s^{-1} for
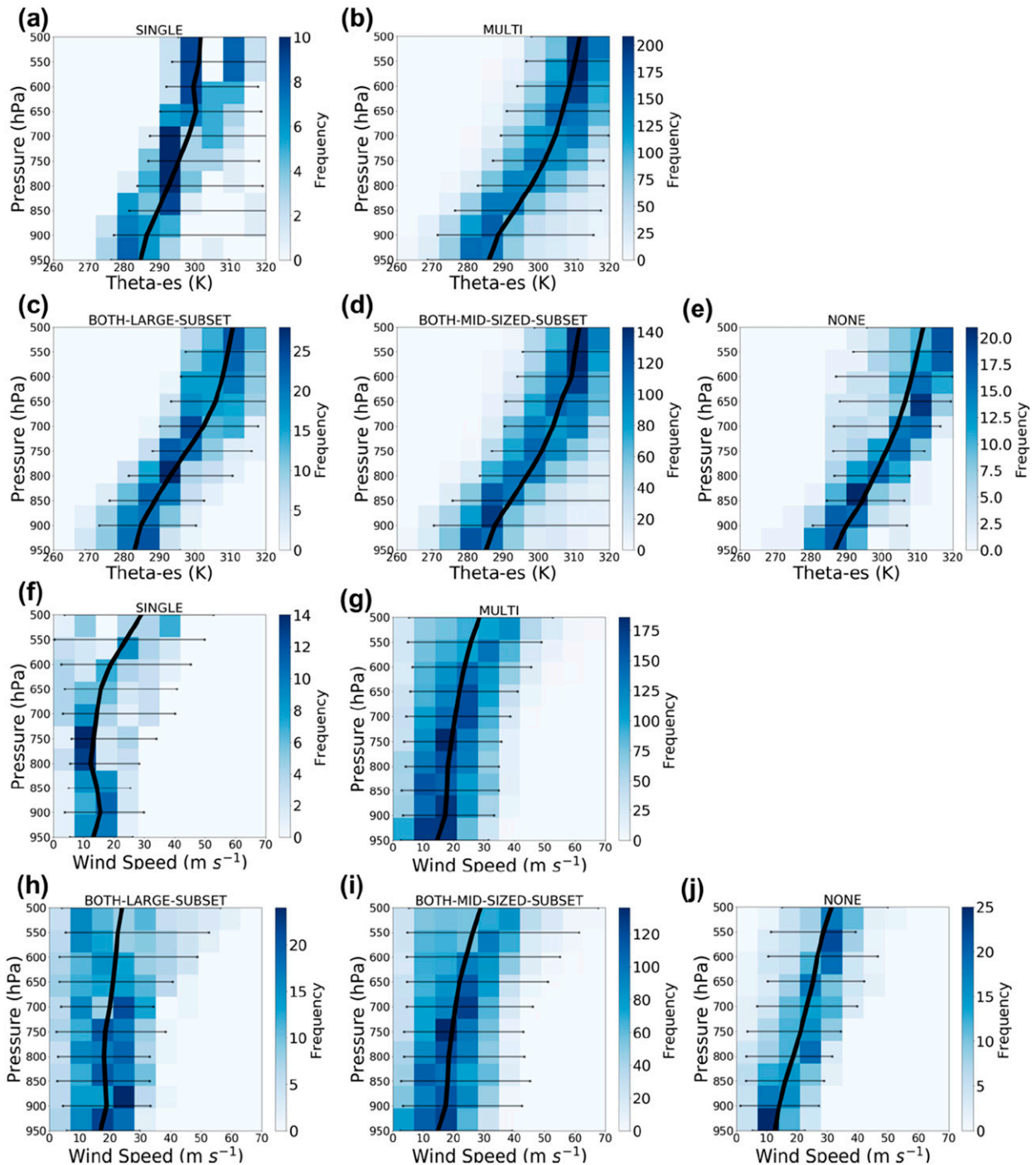
FIG. 7. As in Fig. 6, but for (a)–(e) saturation equivalent potential temperature (K) and (f)–(j) wind speed (kt; 1 kt ≈ 0.5144 m s^{-1}). Red profiles in (a)–(d) indicate those that exhibit a conditionally unstable 50-hPa layer ($d\theta_e^*/dP \leq 0.02$K hPa^{-1}).

SINGLE and BOTH–Large bands, respectively (Fig. 7j; Table 3).

Average profiles of 2D Petterssen (1936) frontogenesis [Eq. (1); as in Novak et al. (2004), their Eq. (1)] were computed for SINGLE and BOTH–Large bands subset

(Figs. 8a,c) and compared to BOTH–Midsized bands subset and MULTI (Figs. 8b,d). Larger, single bands are associated with stronger forcing for lift via frontogenesis than multibands, likely related to their preferential location in the northwest quadrant of low pressure systems (Table 3):

TABLE 3. Environmental banding ingredients for each classification type.

	700-hPa frontogenesis [K $(100\,km)^{-1}\,h^{-1}$]	700-hPa MPV* (PVU)	750–650-hPa dT/dP ($\times 10^{-4}\,°C\,Pa^{-1}$)	750–650-hPa $d\theta_e^*/dP$ ($\times 10^{-4}\,K\,Pa^{-1}$)	950–750-hPa wind speed difference (m s^{-1})
SINGLE	0.90	−0.77	−4.98	4.84	3.71
MULTI	0.13	−0.53	−4.71	5.04	5.84
BOTH–Large bands	0.99	−0.75	−3.08	8.04	3.01
BOTH–Midsized bands	0.14	−0.54	−4.55	5.36	5.67
NONE	0.12	−0.63	−4.68	5.32	10.51

$$F_{2D} = \frac{1}{|\nabla\theta|}\left[-\frac{\partial\theta}{\partial x}\left(\frac{\partial u}{\partial x}\frac{\partial\theta}{\partial x}+\frac{\partial v}{\partial x}\frac{\partial\theta}{\partial y}\right)\right.$$
$$\left.-\frac{\partial\theta}{\partial y}\left(\frac{\partial u}{\partial y}\frac{\partial\theta}{\partial x}+\frac{\partial v}{\partial y}\frac{\partial\theta}{\partial y}\right)\right]. \tag{1}$$

Equation (1) of frontogenesis (F_{2D}) includes the gradients in the zonal (x) and meridional (y) directions of potential temperature (θ) and the zonal and meridional components of the wind (u and v, respectively). Nonbanded and multibanded environments were associated with lower values of frontogenesis than other classifications (Fig. 8).

CSI is indicated by negative values of saturation equivalent potential vorticity [MPV*; Eqs. (2)–(3); McCann 1995] in the absence of inertial and conditional instability (Schultz and Schumacher 1999):

$$MPV^* = \frac{1}{\rho}\boldsymbol{\eta}\cdot\nabla\theta_e^*, \tag{2}$$

$$MPV^* = g\left[\left(\frac{\partial\theta_e^*}{\partial x}\frac{\partial v}{\partial P}\right)-\left(\frac{\partial\theta_e^*}{\partial y}\frac{\partial u}{\partial P}\right)\right.$$
$$\left.-\frac{\partial\theta_e^*}{\partial P}\left(\frac{\partial v}{\partial x}-\frac{\partial u}{\partial y}+f\right)\right], \tag{3}$$

in which g is gravity, P is pressure, f is the Coriolis parameter equal to $2\Omega\sin\phi$ where ϕ is latitude, ρ is the density, $\boldsymbol{\eta}$ is the absolute vorticity vector, and θ_e^* is the saturation equivalent potential temperature. Equation (3) follows from Eq. (2), assuming the horizontal gradient of the vertical wind speed is small and can be neglected. Banded precipitation has been related to CSI (negative MPV*) via the following components of the conceptual model put forth by Clark et al. (2002): 1) a region of midtroposphere frontogenesis over the banded precipitation region, 2) a saturated mesoscale updraft on the warm side of the frontogenesis region, 3) negative MPV production near the updraft dominated by differential vertical θ_e transport, and 4) release of CSI leading to banded precipitation. A negative value for MPV* would indicate the presence of CSI in the absence of CI, a known instability responsible for enhancing circulations associated with some single bands (Novak et al. 2010).

Average profiles of MPV* were calculated from the four closest grid points centered on the band location for all vertical levels. CSI is evident in the average profiles of all classification types below 600 hPa (Figs. 8f–i). The most negative values in the average profiles of MPV* are found between 900 and 800 hPa for all classifications, with MPV* < 0 and statistically insignificant differences among the classifications between 700 and 550 hPa (Fig. 8j).

Looking at one particular level (e.g., 700 hPa), frontogenesis was calculated along with the 750–650-hPa layer-averaged value of MPV* (Fig. 9). The NONE, MULTI, and BOTH–Midsized bands events exhibit the weakest frontogenesis [<2 K $(100\,km)^{-1}$ $(1\,h)^{-1}$]. BOTH–Large bands events had the largest frontogenetical values with 12 of 107 (~11%) events associated with frontogenesis >1.5 K $(100\,km)^{-1}$ $(1\,h)^{-1}$. The MULTI environment showed relatively weak frontogenesis values with 34 events <1.5 K $(100\,km)^{-1}$ $(1\,h)^{-1}$. Two BOTH–Midsized bands events exhibited 700–600-hPa conditionally unstable layers (θ_e^* decreasing with height), but 99 of 107 (93%) events were associated with moist symmetric instability (MPV* < 0). None of the MULTI events exhibited conditional instability, but 34 events exhibited conditional symmetric instability. SINGLE and BOTH–Large bands subset classifications exhibited more layers of CI than NONE, MULTI, and BOTH–Midsized bands subset (not shown).

A simple frontogenesis threshold does not distinguish among band categories, as shown in Fig. 10. While SINGLE and BOTH–Large bands occurred in environments of strong frontogenesis, they also occurred with moderate and weak frontogenesis. MULTI, BOTH–Midsized bands, and NONE occurred in conditions of moderate to weak frontogenesis. The combination of MPV and frontogenesis does not clearly distinguish among band categories either. Hence, while the presence of strong frontogenesis increases the likelihood of a single band forming, these long bands as well as shorter multibands do form in weaker forcing conditions.

5. Summary and discussion

A combination of objective and subjective approaches for the classification of bands of 108 NEUS winter storms
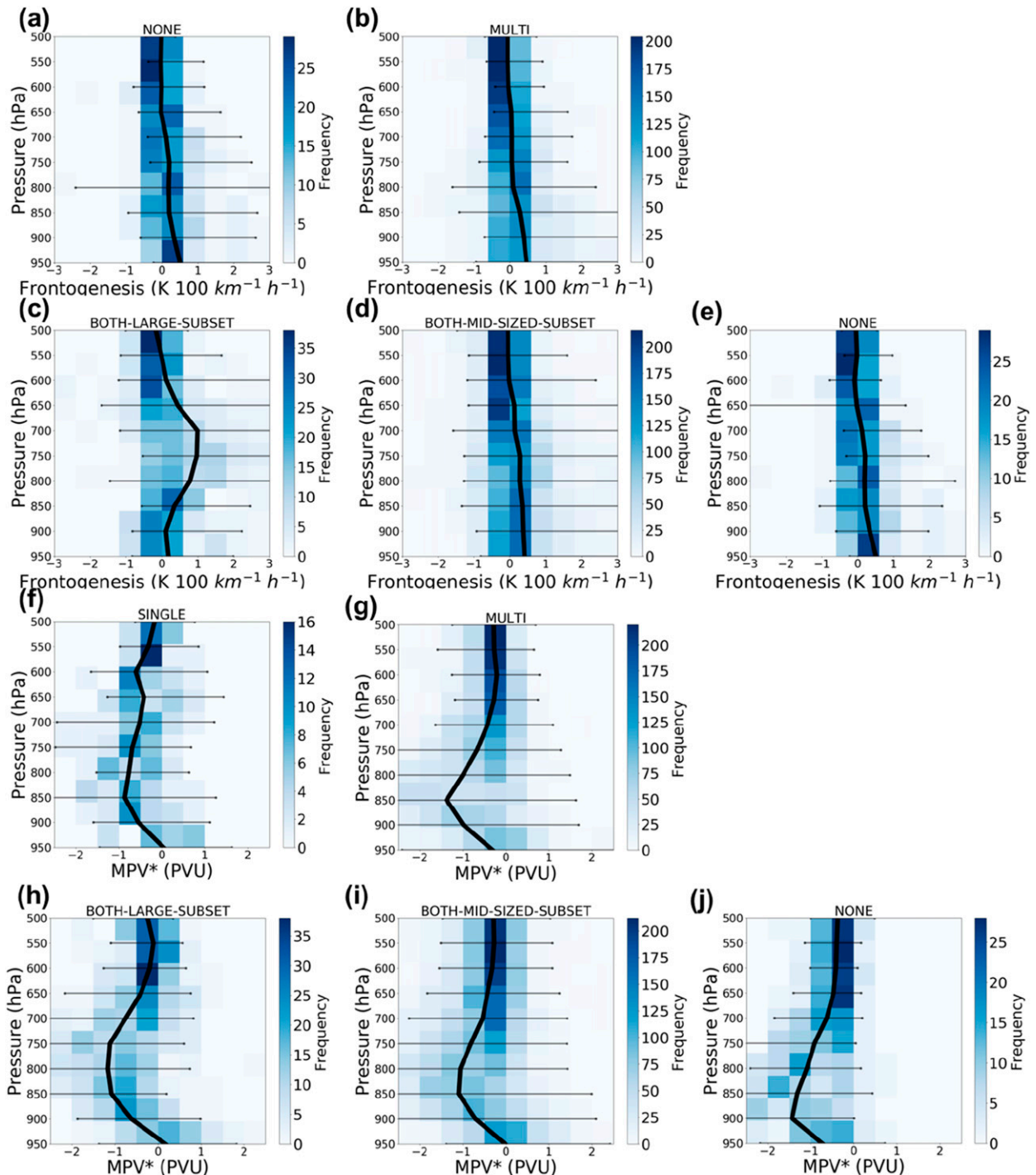
FIG. 8. As in Fig. 6, but for (a)–(e) frontogenesis [K $(100 \, km)^{-1} \, h^{-1}$] and (f)–(j) saturation equivalent potential vorticity (MPV*; PVU).

from 1996 to 2016 was conducted. This is the first formal attempt to automatically identify bands within winter storms using a feature-based algorithm. The dataset comprised extratropical cyclones that produced ≥1.00 in. (2.54 cm) per day liquid equivalent snowfall at ≥2 of 7

ASOS stations along the eastern seaboard from Delaware to Maine. Regional composite 2-km AGL radar reflectivity data from six coastal NEUS radars were used to identify and classify bands using the Model Evaluation Tools (MET) Method for Object-based Diagnostic
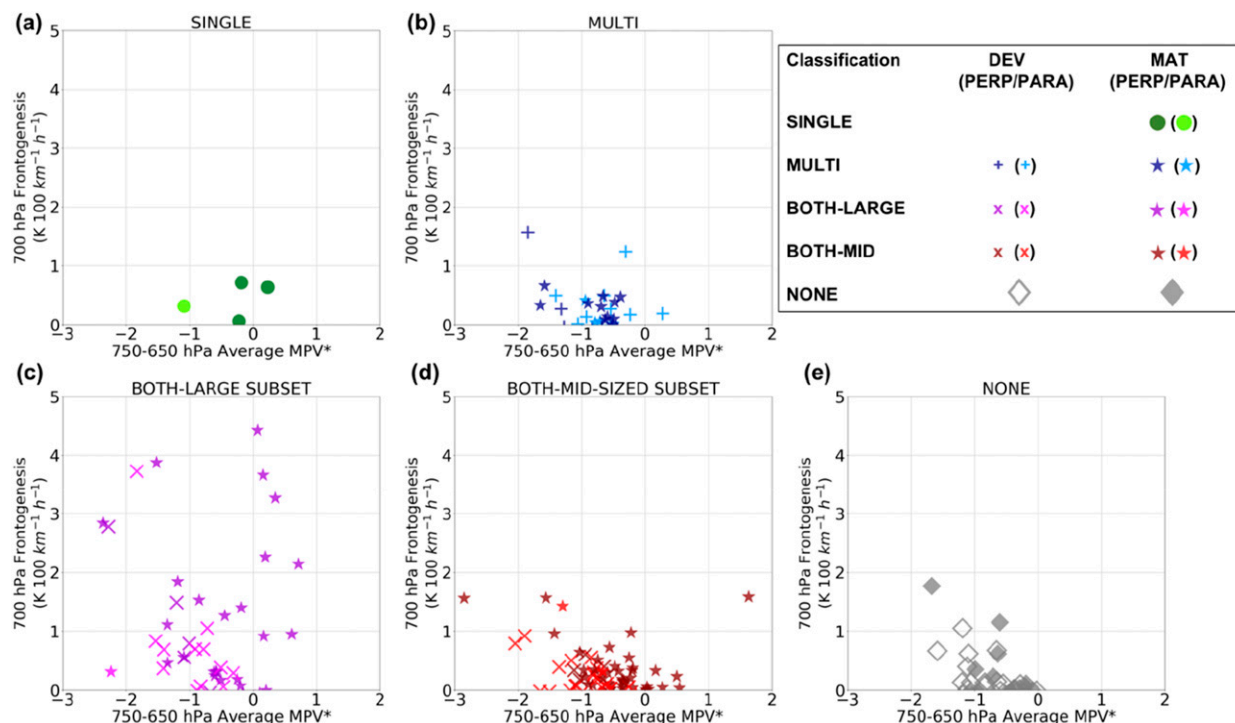
FIG. 9. The relationship between 750–650-hPa-averaged saturation equivalent potential vorticity (MPV*; PVU) on the abscissa and 700-hPa frontogenesis [K $(100\,km)^{-1}\,h^{-1}$] on the ordinate for (a) SINGLE, (b) MULTI, (c) BOTH–Large bands subset, (d) BOTH–Midsized bands subset, and (e) NONE classified events from developing (DEV) or mature (MAT) cyclones exhibiting perpendicular (PERP) or parallel (PARA) band motion.

Evaluation (MODE), specifically into large bands ($L \geq 200\,km$) and midsized bands ($L < 200\,km$), both with aspect ratios (ratio of width to length) ≤ 0.5. At each 6-hourly analysis time, the portions of the storm falling within each of six $300\,km \times 300\,km$ boxes centered on operational sounding sites were categorized as containing a single band only (SINGLE), multibands only (MULTI), both single and multibands (BOTH), or nonbanded (NONE) for radar echoes present in $\geq 50\%$ of the box $\geq 2\,h$. This resulted in 193 classified storm subperiods from 108 storms, with the most common categories being BOTH (107) and NONE (46), followed by MULTI (35) and SINGLE (5) (Table 2). This study found that single bands unaccompanied by multibands are actually quite rare, compared to the findings of previous studies. This discrepancy is likely a result of the 5-dBZ binning of the reflectivity field that others used, compared to our analysis that used 0.5-dB precision level-II radar data and a method that detected locally enhanced features relative to a changing background.
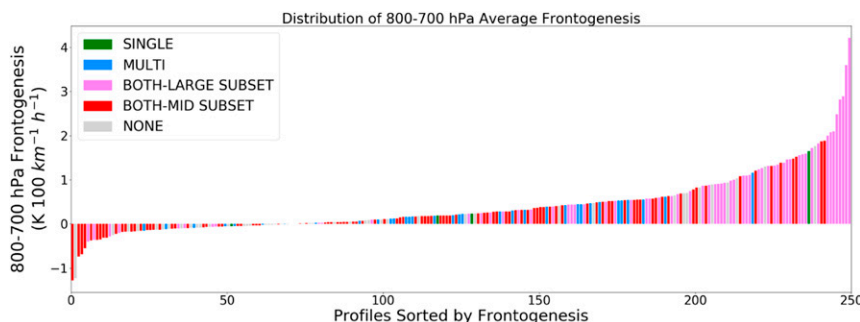

FIG. 10. Distribution of 800–700-hPa average frontogenesis for all events in the dataset colored by classification as SINGLE (green), MULTI (blue), BOTH–Large bands subset (magenta), BOTH–Midsized bands subset (red), or NONE (gray).

Additional information was used to further subclassify the categories by their association with a developing or mature cyclone and the type of geographic-centric band movement exhibited as either moving perpendicular to the long axis or moving parallel to the long axis. Developing cyclones were predominantly associated with parallel-moving bands (69%) that were clustered in the northeast quadrant. Mature cyclones most often exhibited BOTH (48%) in the northwest quadrant, MULTI (17%) in the northeast quadrant, NONE (17%) in the eastern quadrants, and SINGLE (5%) in the northwest quadrant. Mature cyclones were predominantly associated with perpendicular-moving bands (87%) that occurred most frequently in the northwest quadrant of the cyclone.

CFSR and CFSv2 analyses were used to compare environmental variables of the known important single-banding ingredients of lift, instability, and moisture for the different banding classifications. Strong frontogenesis increases the likelihood of a single band forming, but these long bands as well as shorter multibands can form in an environment of weak frontogenesis. This suggests that given an environment of weak frontogenesis, other lifting processes may need to be explored, such as gravity waves or vertical shear instabilities. MULTI and BOTH–Large bands profiles exhibited larger 1000–700-hPa wind shear, compared to SINGLE and BOTH–Large bands, and the importance of this result will be explored in a future case study.

MULTI and BOTH–Midsized bands typically exhibit a 200-hPa layer of conditional symmetric instability (CSI; indicated by MPV* < 0 PVU; 1 PVU = $10^{-6}\,\mathrm{K\,kg^{-1}\,m^2\,s^{-1}}$) more often than conditional instability (CI). Previous studies suggest that CSI is the dominant instability responsible for multiple bands from analysis of one case or synoptic situation (e.g., Shields et al. 1991; Xu 1992) to three cases (Nicosia and Grumm 1999). Furthermore, precipitation bands are not always associated with CSI (Schultz and Schumacher 1999). Novak et al. (2010) found that CI occurred more often than CSI near the time of band formation for dozens of single-band cases within mature cyclones. In this study, we analyze all times when bands are present, which includes formation, development, maturation, and dissipation. CSI was evident in the average profiles of all classification types below 600 hPa (Figs. 8f–i), but CI was more associated with SINGLE and BOTH–Large bands rather than MULTI and BOTH–Midsized bands. In particular, CSI was more common than CI between 900 and 800 hPa among all five classifications. NONE events show shallow near-surface layers of CSI, but it might not be released without lifting via frontogenesis. There was no significant difference in the third banding ingredient—moisture—among the classifications, likely due to the common location in the near-saturated environment of the cyclone comma head. General differences among banded environments are provided in this paper. Future work could utilize both observations and a high-resolution mesoscale model to explore some of the mechanisms for multiband development, as well as to analyze the evolutions of single and multibands, separately, to examine differences in more detail.

REFERENCES

Baxter, M., and P. Schumacher, 2017: Distribution of single-banded snowfall in central U.S. cyclones. *Wea. Forecasting*, **32**, 533–554, https://doi.org/10.1175/WAF-D-16-0154.1.

Bjerknes, J., and H. Solberg, 1922: Life cycle of cyclones and the polar front theory of atmospheric circulation. *Geofys. Publ.*, **3**, 3–18.

Brown, B. G., R. Bullock, J. Halley Gotway, D. Ahijevych, C. Davis, E. Gilleland, and L. Holland, 2007: Application of the MODE object-based verification tool for the evaluation of model precipitation fields. *22nd Conf. on Weather Analysis and Forecasting/18th Conf. on Numerical Weather Prediction*, Park City, UT, Amer. Meteor. Soc., 10A.2, https://ams.confex.com/ams/22WAF18NWP/techprogram/paper_124856.htm.

Bullock, R. G., B. G. Brown, and T. L. Fowler, 2016: Method for object-based diagnostic evaluation. NCAR Tech. Note NCAR/TN-532+STR, 84 pp., https://doi.org/10.5065/D61V5CBS.

Charles, M. E., and B. A. Colle, 2009: Verification of extratropical cyclones within the NCEP operational models. Part I: Analysis errors and short-term NAM and GFS forecasts. *Wea. Forecasting*, **24**, 1173–1190, https://doi.org/10.1175/2009WAF2222169.1.

Clark, J. H. E., R. P. James, and R. H. Grumm, 2002: A re-examination of the mechanisms responsible for banded precipitation. *Mon. Wea. Rev.*, **130**, 3074–3086, https://doi.org/10.1175/1520-0493(2002)130<3074:AROTMR>2.0.CO;2.

Colle, B. A., Z. Zhang, K. A. Lombardo, E. Chang, P. Liu, and M. Zhang, 2013: Historical evaluation and future prediction of eastern North American and western Atlantic extratropical cyclones in the CMIP5 models during the cool season. *J. Climate*, **26**, 6882–6903, https://doi.org/10.1175/JCLI-D-12-00498.1.

——, D. Stark, and S. E. Yuter, 2014: Surface microphysical observations within East Coast winter storms on Long Island, New York. *Mon. Wea. Rev.*, **142**, 3126–3146, https://doi.org/10.1175/MWR-D-14-00035.1.

Corbin, N. A., 2016: Northern California's Central Valley spatial precipitation patterns associated with atmospheric rivers under different environmental conditions. M.S. thesis, Dept. of Marine, Earth, and Atmospheric Sciences, North Carolina State University, 227 pp., http://www.lib.ncsu.edu/resolver/1840.16/10999.

Davis, C. A., B. G. Brown, and R. G. Bullock, 2006a: Object-based verification of precipitation forecasts. Part I: Methodology and application to mesoscale rain areas. *Mon. Wea. Rev.*, **134**, 1772–1784, https://doi.org/10.1175/MWR3145.1.

——, ——, and ——, 2006b: Object-based verification of precipitation forecasts. Part II: Application to convective rain systems. *Mon. Wea. Rev.*, **134**, 1785–1795, https://doi.org/10.1175/MWR3146.1.

Developmental Testbed Center, 2015: Model Evaluation Tools version 5.1 (METv5.1) user's guide. Developmental Testbed Center Rep., 317 pp., https://dtcenter.org/met/users/docs/users_guide/MET_Users_Guide_v5.1.pdf.

Emanuel, K. A., 1985: Frontal circulations in the presence of small moist symmetric stability. *J. Atmos. Sci.*, **42**, 1062–1071, https://doi.org/10.1175/1520-0469(1985)042<1062:FCITPO>2.0.CO;2.

Fairman, J. G., Jr., D. M. Schultz, D. J. Kirshbaum, S. L. Gray, and A. I. Barrett, 2016: Climatology of banded precipitation over the contiguous United States. *Mon. Wea. Rev.*, **144**, 4553–4568, https://doi.org/10.1175/MWR-D-16-0015.1.

Ganetis, S., and B. Colle, 2015: The thermodynamic and microphysical evolution of an intense snowband during the northeast U.S. blizzard of 8–9 February 2013. *Mon. Wea. Rev.*, **143**, 4104–4125, https://doi.org/10.1175/MWR-D-14-00407.1.

Hoban, N. P., 2016: Observed characteristics of mesoscale banding in coastal northeast U.S. snow storms. M.S. thesis, Dept. of Marine, Earth, and Atmospheric Sciences, North Carolina State University, 66 pp., http://www.lib.ncsu.edu/resolver/1840.20/33405.

Hodges, K. I., 1995: Feature tracking on the unit sphere. *Mon. Wea. Rev.*, **123**, 3458–3465, https://doi.org/10.1175/1520-0493(1995)123<3458:FTOTUS>2.0.CO;2.

Jurewicz, M. L., and M. S. Evans, 2004: A comparison of two banded, heavy snowstorms with very different synoptic settings. *Wea. Forecasting*, **19**, 1011–1028, https://doi.org/10.1175/WAF-823.1.

Kenyon, J. S., 2013: The motion of mesoscale snowbands in northeast U.S. winter storms. M.S. thesis, Dept. of Atmospheric and Environmental Sciences, University at Albany, State University of New York, 108 pp., http://www.atmos.albany.edu/student/jkenyon/Kenyon_thesis.pdf.

Kocin, P., L. W. Uccellini, J. Alpert, B. Ballish, D. Bright, R. Grumm, and G. Manikin, 2011: The blizzard of 25–27 December 2010: Forecast assessment. NOAA/NCEP event review, 57 pp., http://www.wpc.ncep.noaa.gov/winter_storm_summaries/event_reviews/2010/December25_27_2010_Blizzard.pdf.

Krekeler, J., 2013: Great Lakes to Northeast major winter storm. NOAA/NCEP/WPC event review, 2 pp., http://www.wpc.ncep.noaa.gov/winter_storm_summaries/event_reviews/2013/Great_Lakes_Northeast_Winter_Storm_Feb2013.pdf.

Lawson, J. R., and W. A. Gallus, 2016: Adapting the SAL method to evaluate reflectivity forecasts of summer precipitation in the central United States. *Atmos. Sci. Lett.*, **17**, 524–530, https://doi.org/10.1002/asl.687.

McCann, D. W., 1995: Three-dimensional computations of equivalent potential vorticity. *Wea. Forecasting*, **10**, 798–802, https://doi.org/10.1175/1520-0434(1995)010<0798:TDCOEP>2.0.CO;2.

Moore, J. T., C. E. Graves, S. Ng, and J. L. Smith, 2005: A process-oriented methodology toward understanding the organization of an extensive mesoscale snowband: A diagnostic case study of 4–5 December 1999. *Wea. Forecasting*, **20**, 35–50, https://doi.org/10.1175/WAF-829.1.

Nicosia, D. J., and R. H. Grumm, 1999: Mesoscale band formation in three major northeastern United States snowstorms. *Wea. Forecasting*, **14**, 346–368, https://doi.org/10.1175/1520-0434(1999)014<0346:MBFITM>2.0.CO;2.

Novak, D. R., and B. A. Colle, 2012: Diagnosing snowband predictability using a multimodel ensemble system. *Wea. Forecasting*, **27**, 565–585, https://doi.org/10.1175/WAF-D-11-00047.1.

——, L. F. Bosart, D. Keyser, and J. S. Waldstreicher, 2004: An observational study of cold season–banded precipitation in northeast U.S. cyclones. *Wea. Forecasting*, **19**, 993–1010, https://doi.org/10.1175/815.1.

——, B. A. Colle, and S. E. Yuter, 2008: High-resolution observations and model simulations of the life cycle of an intense mesoscale snowband over the northeastern United States. *Mon. Wea. Rev.*, **136**, 1433–1456, https://doi.org/10.1175/2007MWR2233.1.

——, ——, and R. McTaggart-Cowan, 2009: The role of moist processes in the formation and evolution of mesoscale snowbands within the comma head of northeast U.S. cyclones. *Mon. Wea. Rev.*, **137**, 2662–2686, https://doi.org/10.1175/2009MWR2874.1.

——, ——, and A. R. Aiyyer, 2010: Evolution of mesoscale precipitation band environments within the comma head of northeast U.S. cyclones. *Mon. Wea. Rev.*, **138**, 2354–2374, https://doi.org/10.1175/2010MWR3219.1.

Petterssen, S., 1936: Contribution to the theory of frontogenesis. *Geofys. Publ.*, **11** (6), 1–27.

Picca, J. C., D. M. Schultz, B. A. Colle, S. Ganetis, D. R. Novak, and M. Sienkiewicz, 2014: The value of dual-polarization radar in diagnosing the complex microphysical evolution of an intense snowband. *Bull. Amer. Meteor. Soc.*, **95**, 1825–1834, https://doi.org/10.1175/BAMS-D-13-00258.1.

Saha, S., and Coauthors, 2010: The NCEP Climate Forecast System Reanalysis. *Bull. Amer. Meteor. Soc.*, **91**, 1015–1058, https://doi.org/10.1175/2010BAMS3001.1.

——, and Coauthors, 2014: The NCEP Climate Forecast System version 2. *J. Climate*, **27**, 2185–2208, https://doi.org/10.1175/JCLI-D-12-00823.1.

Sanders, F., and L. F. Bosart, 1985a: Mesoscale structure in the megalopolitan snowstorm of 11–12 February 1983. Part I: Frontogenetical forcing and symmetric instability. *J. Atmos. Sci.*, **42**, 1050–1061, https://doi.org/10.1175/1520-0469(1985)042<1050:MSITMS>2.0.CO;2.

——, and ——, 1985b: Mesoscale structure in the megalopolitan snowstorm, 11–12 February 1983. Part II: Doppler radar study of the New England snowband. *J. Atmos. Sci.*, **42**, 1398–1407, https://doi.org/10.1175/1520-0469(1985)042<1398:MSITMS>2.0.CO;2.

Schultz, D. M., and P. N. Schumacher, 1999: The use and misuse of conditional symmetric instability. *Mon. Wea. Rev.*, **127**, 2709–2732, https://doi.org/10.1175/1520-0493(1999)127<2709:TUAMOC>2.0.CO;2.

——, and G. Vaughan, 2011: Occluded fronts and the occlusion process: A fresh look at conventional wisdom. *Bull. Amer. Meteor. Soc.*, **92**, 443–466, https://doi.org/10.1175/2010BAMS3057.1.

Shapiro, M. A., and D. Keyser, 1990: Fronts, jet streams and the tropopause. *Extratropical Cyclones: The Erik Palmén Memorial Volume*, C. W. Newton and E. O. Holopainen, Eds., Amer. Meteor. Soc., 167–191.

Shields, M. T., R. M. Rauber, and M. K. Ramamurthy, 1991: Dynamical forcing and mesoscale organization of precipitation bands in a Midwest winter cyclonic storm. *Mon. Wea. Rev.*, **119**, 936–964, https://doi.org/10.1175/1520-0493(1991)119<0936:DFAMOO>2.0.CO;2.

Soltow, M., 2011: December 25–27, 2010 winter storm, eastern United States. NOAA/NCEP/WPC event review, 13 pp., http://www.wpc.ncep.noaa.gov/winter_storm_summaries/event_reviews/2010/Eastern_US_WinterStorm_December_2010.pdf.

Thorpe, A. J., and K. A. Emanuel, 1985: Frontogenesis in the presence of small stability to slantwise convection. *J. Atmos. Sci.*,

42, 1809–1824, https://doi.org/10.1175/1520-0469(1985)042<1809:FITPOS>2.0.CO;2.

Wilks, D. S., 2011: *Statistical Methods in the Atmospheric Sciences*. 3rd ed. International Geophysics Series, Vol. 100, Academic Press, 704 pp.

Wolfsberg, D. G., K. A. Emanuel, and R. E. Passarelli, 1986: Band formation in a New England winter storm. *Mon. Wea. Rev.*, **114**, 1552–1569, https://doi.org/10.1175/1520-0493(1986)114<1552:BFIANE>2.0.CO;2.

Xu, Q., 1989: Extended Sawyer–Eliassen equation for frontal circulations in the presence of small viscous moist symmetric stability. *J. Atmos. Sci.*, **46**, 2671–2683, https://doi.org/10.1175/1520-0469(1989)046<2671:ESEFFC>2.0.CO;2.

——, 1992: Formation and evolution of frontal rainbands and geostrophic potential vorticity anomalies. *J. Atmos. Sci.*, **49**, 629–648, https://doi.org/10.1175/1520-0469(1992)049<0629:FAEOFR>2.0.CO;2.